

Elucidating Individual Magnetic Contributions in Bi-Magnetic Fe₃O₄/Mn₃O₄ Core/Shell Nanoparticles by Polarized Powder Neutron Diffraction

I. V. Golosovsky, I. A. Kibalin, A. Gukasov, A. G. Roca, A. López-Ortega, M. Estrader, M. Vasilakaki, K. N. Trohidou, T. C. Hansen, I. Puente-Orench, E. Lelièvre-Berna, and J. Nogués*

Heterogeneous bi-magnetic nanostructured systems have had a sustained interest during the last decades owing to their unique magnetic properties and the wide range of derived potential applications. However, elucidating the details of their magnetic properties can be rather complex. Here, a comprehensive study of Fe₃O₄/Mn₃O₄ core/shell nanoparticles using polarized neutron powder diffraction, which allows disentangling the magnetic contributions of each of the components, is presented. The results show that while at low fields the Fe₃O₄ and Mn₃O₄ magnetic moments averaged over the unit cell are antiferromagnetically coupled, at high fields, they orient parallel to each other. This magnetic reorientation of the Mn₃O₄ shell moments is associated with a gradual evolution with the applied field of the local magnetic susceptibility from anisotropic to isotropic. Additionally, the magnetic coherence length of the Fe₃O₄ cores shows some unusual field dependence due to the competition between the antiferromagnetic interface interaction and the Zeeman energies. The results demonstrate the great potential of the quantitative analysis of polarized neutron powder diffraction for the study of complex multiphase magnetic materials.

1. Introduction

During the last decades magnetic nanostructured materials composed of two or more magnetic phases (e.g., composite nanoparticle assemblies, nanoparticles in matrices or core/shell nanoparticles) have been extensively studied both from fundamental and applied viewpoints.^[1–16] From a basic science perspective, issues like dipolar and exchange interactions, collective behavior, magnetic graded interfaces, proximity effects, among many others, have been investigated. Additionally, bi-magnetic materials are being studied for countless applications, like biomedical uses (e.g., magnetic hyperthermia and magnetic resonance imaging), permanent magnets, magnetic recording, magnetic refrigeration, or microwave absorption.^[1–16]

The most common technique to study these materials is magnetometry. However, magnetization measurements usually cannot discern between the different

I. V. Golosovsky
National Research Center “Kurchatov Institute”
B. P. Konstantinov Petersburg Nuclear Physics Institute
Gatchina 188300, Russia
I. A. Kibalin, A. Gukasov
Laboratoire Léon Brillouin
CEA-CNRS
CE-Saclay
Gif-sur-Yvette 91191, France

A. G. Roca, J. Nogués
Catalan Institute of Nanoscience and Nanotechnology (ICN2)
CSIC and BIST
Campus UAB, Bellaterra, Barcelona 08193, Spain
E-mail: josep.nogues@icn2.cat
A. López-Ortega
Departamento de Ciencias
Universidad Pública de Navarra
Pamplona 31006, Spain
A. López-Ortega
Institute for Advanced Materials and Mathematics INAMAT2
Universidad Pública de Navarra
Pamplona 31006, Spain
M. Estrader
Departament de Química Inorgànica i Orgànica
carrer Martí i Franqués 1–11
Universitat de Barcelona
Barcelona 08028, Spain

 The ORCID identification number(s) for the author(s) of this article can be found under <https://doi.org/10.1002/smt.202201725>

© 2023 The Authors. Small Methods published by Wiley-VCH GmbH. This is an open access article under the terms of the Creative Commons Attribution-NonCommercial License, which permits use, distribution and reproduction in any medium, provided the original work is properly cited and is not used for commercial purposes.

DOI: 10.1002/smt.202201725

contributions of the diverse magnetic components, although in some cases, indirect information about the magnetic phases can be obtained using more advanced analyses like Henkel plots or first-order reversal curves.^[14,17]

To obtain some information about the contribution of each magnetic phase a number of techniques can be used, like neutron diffraction,^[12,18–20] X-ray magnetic circular dichroism (XMCD), and derived methods such as X-ray photoemission electron microscopy or X-ray microscopy,^[21–23] small angle neutron scattering (SANS),^[24–26] electron magnetic circular dichroism (e-MCD),^[27,28] Mössbauer spectroscopy,^[20,29,30] among others. Each of these methods has its advantages and drawbacks. For example, although XMCD or SANS can provide quantitative information about the magnetic moment, they bear only limited structural information (e.g., crystallographic phases) about the components, e-MCD can only be used on very thin samples or Mössbauer spectroscopy is basically restricted to Fe-based materials. Hence, the interpretation of the magnetic behavior of multicomponent magnetic materials is often challenging and frequently a combination of different techniques is necessary to understand the insights of their magnetic properties. In this framework, novel approaches can be very valuable to help in the understanding of the complex magnetic properties of composite nanostructured magnetic systems.

Here, we demonstrate that polarized neutron powder diffraction (PNPD) is a valuable tool to acquire unique information, difficult or impossible to retrieve with other techniques, from bimagnetic nanostructured systems (i.e., Fe₃O₄/Mn₃O₄ core/shell nanoparticles). In particular, the results demonstrate that distinct magnetic features of the two different counterparts can easily be obtained using with PNPD.

Polarized neutron diffraction consists in measuring neutron structure factors using an incident neutron beam polarized parallel (spin-up) and anti-parallel (spin-down) to a vertically applied magnetic field.^[19,31,32] Unlike neutron diffraction with an unpolarized beam, this method is sensitive at determining a magnetization distribution within a unit cell, as well as the local susceptibility tensor at each magnetic site,^[19,31,32] and has been extensively used with single crystals.^[19,31–35] However, PNPD has been only seldom used in polycrystalline structures,^[31,32,36–42] because of the weak diffraction signal and there was until recently

no software to properly analyze the data. The weak diffraction signal is exacerbated in nanostructured systems since the broadening of the diffraction peaks reduces even further the signal-to-background ratio. However, improvements made in neutron instrumentation^[32] (focusing monochromators, ³He spin filters, high field magnets, position sensitive detectors) and the event of a new software,^[43] which has already been successfully applied to data treatment of different compounds,^[44,45] make PNPD much more attractive.

2. Results and Discussion

Two different Fe₃O₄/Mn₃O₄ core/shell nanoparticles have been studied (with different core sizes and shell thickness; see Experimental Section). The transmission electron microscopy (TEM) images (**Figure 1a–h**) show that the particles have a somewhat irregular shape with average sizes of 14.8 ± 2.3 nm (sample 1) and 13.0 ± 1.5 nm (sample 2), respectively. The electron energy loss spectroscopy (EELS; **Figure 1d,h**) analysis of the samples evidences that the particles have a roughly spherical Fe₃O₄ core with a diameter of ≈13 nm (sample 1) and ≈10 nm (sample 2), respectively. On the other hand, the Mn₃O₄ shell is rather inhomogeneous with thicknesses of ≈0.4–1.5 nm (sample 1) and ≈0.7–2.1 nm (sample 2).

To disentangle the contributions of Fe₃O₄ and Mn₃O₄ on the magnetic properties of the samples, a detailed PNPD study at 5 K in different applied fields was carried out. As a first step, to determine the nuclear structure data (lattice parameters, site occupancies, and so on) two different approaches were carried out. For sample 1, the sum of the spin-up and spin-down polarization patterns (equivalent to unpolarized powder diffraction measurements) was used (**Figure 2a,b**) (refined using CrysPy, see Experimental section). For sample 2 (for which the polarized sum profile cannot be refined reliably), the conventional neutron powder diffraction was analyzed by a usual Rietveld procedure (using FullProf; see Experimental Section). As expected, the Fe₃O₄ cores present an inverse cubic spinel structure (space group Fd $\bar{3}$ m; i.e., stoichiometric magnetite for sample 1 and close to stoichiometric maghemite for sample 2), whereas the Mn₃O₄ shells have a normal tetragonal spinel structure (space group I4₁/amd).

The refined core sizes (from the peak broadening; see **Table 1**) are consistent with the ones obtained from TEM. Concerning the shell size, it is difficult to obtain a reliable value from diffraction data because of the overlapping of the peaks from the shell and the core, and the small contribution of a shell to the pattern, which is further complicated by the anisotropic (platelet-like) shape of the shell particles. Thus, in order to estimate approximately the “average thickness” of the shell, the volume fraction of the two phases obtained from the refinement was used assuming a uniform shell on a spherical core. The thicknesses obtained from this approach give only indicative trends and cannot be readily compared with the estimates obtained from the TEM-EELS study. Although the estimated thicknesses are exceedingly small, what is clearly illustrated is that the sample 1 has a thinner shell than sample 2 (**Table 1**), in agreement with the EELS analysis of the samples (**Figure 1d,h**).

In our case, the diffraction signal of the difference pattern (spin up – spin down) has a rather weak signal due to the small amount of sample (see **Figure 2** and **Figure S1**, Supporting

M. Estrader
Institut de Nanociència i Nanotecnologia IN2UB
carrer Martí i Franqués 1–11
Universitat de Barcelona
Barcelona 08028, Spain

M. Vasilakaki, K. N. Trohidou
Institute of Nanoscience and Nanotechnology
NCSR “Demokritos”
153 10, Agia Paraskevi, Attiki 15310, Greece

T. C. Hansen, I. Puente-Orench, E. Lelièvre-Berna
Institut Laue Langevin
71 avenue des Martyrs, Grenoble 38000, France

I. Puente-Orench
Instituto de NanoCiencia y Materiales de Aragón
Zaragoza 50009, Spain

J. Nogués
ICREA
Barcelona 08010, Spain

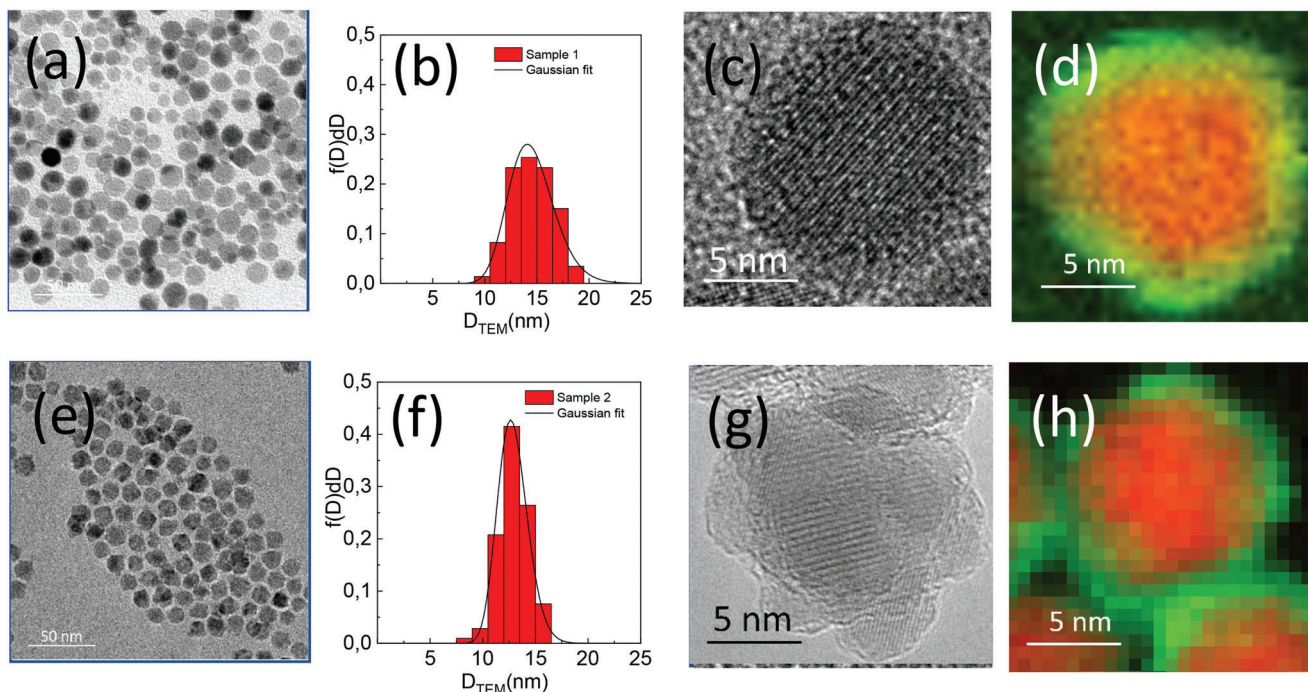


Figure 1. Low-resolution TEM images, particle size distribution, high-resolution TEM image and Fe (red) and (green) Mn L-edge EELS mapping for a–d) sample 1 and e–h) sample 2.

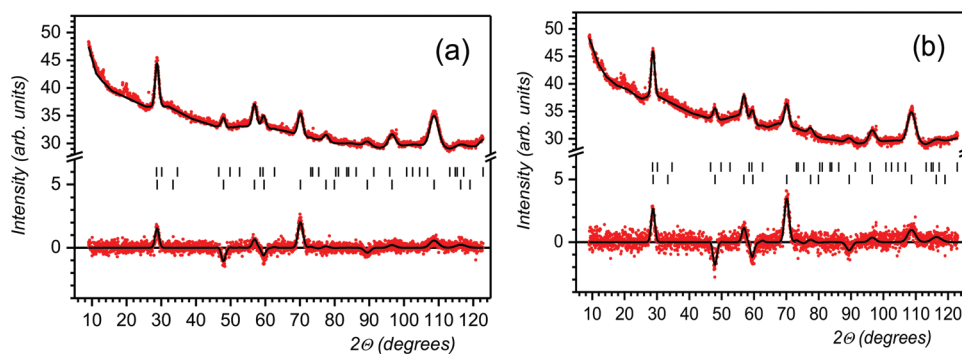


Figure 2. Refinement of the sum (spin up + spin down; top curves) and difference (spin up – spin down; bottom curves) of the spin-up and spin-down pattern for sample 1 at a) 5 kOe and b) 50 kOe. The bars indicate the position of diffraction reflections for Mn_3O_4 (top row) and Fe_3O_4 (bottom row) (see Supporting Information).

Information) and, consequently, the Rietveld profile analysis (using CrysPy; see Experimental Section) does not provide univocal results. Therefore, to simplify the fitting procedure (i.e., introducing some constraints in the magnetic structure to reduce the number of fitting parameters), a novel approach combining the PNPd refinement and magnetization measurements has been used. Namely, to check the consistency of the model used in the fitting procedure (i.e., a simplified model of the magnetic structure; see Experimental Section), the refined moment averaged over the whole system ($m_{\text{Fe}_3\text{O}_4} + m_{\text{Mn}_3\text{O}_4}$) was compared to superconducting quantum interference device (SQUID) magnetization measurements. When the appropriate refined model is defined, the field evolution of the magnetization calculated from

the diffraction and the one obtained from SQUID measurements are similar (see Experimental Section for details).

Notably, the fit of the patterns allows to separate the field dependence of the magnetic moments of the two phases in a straightforward way. Note that the small differences in the magnetic moments averaged over the unit cell for the two iron oxide cores originate from the different iron oxide phases of the cores (sample 1—magnetite versus sample 2—maghemite). As can be seen in **Figure 3a,b**, the refined magnetic moments averaged over the unit cell (i.e., the projection of the moment onto the applied field direction) unambiguously demonstrate that the moments averaged over the unit cells of the Fe_3O_4 and its Mn_3O_4 counterpart are antiferromagnetically coupled at low fields for both

Table 1. Refined parameters from the neutron powder diffraction of samples 1 and 2 at 5 K in zero field. The errors given in brackets are standard deviations obtained using the FullProf and CrysPy programs.

Name	Core			Shell			Average thickness [nm]
	a [Å]	Size [nm]	Volume fraction (%)	a [Å]	c [Å]	Volume fraction [%]	
Sample 1	8.354(1)	10.5(5)	87(2)	5.698(4)	9.23(2)	12(2)	0.2
Sample 2	8.336(1)	7.7(5)	73(3)	5.723(6)	9.48(3)	27(2)	0.4

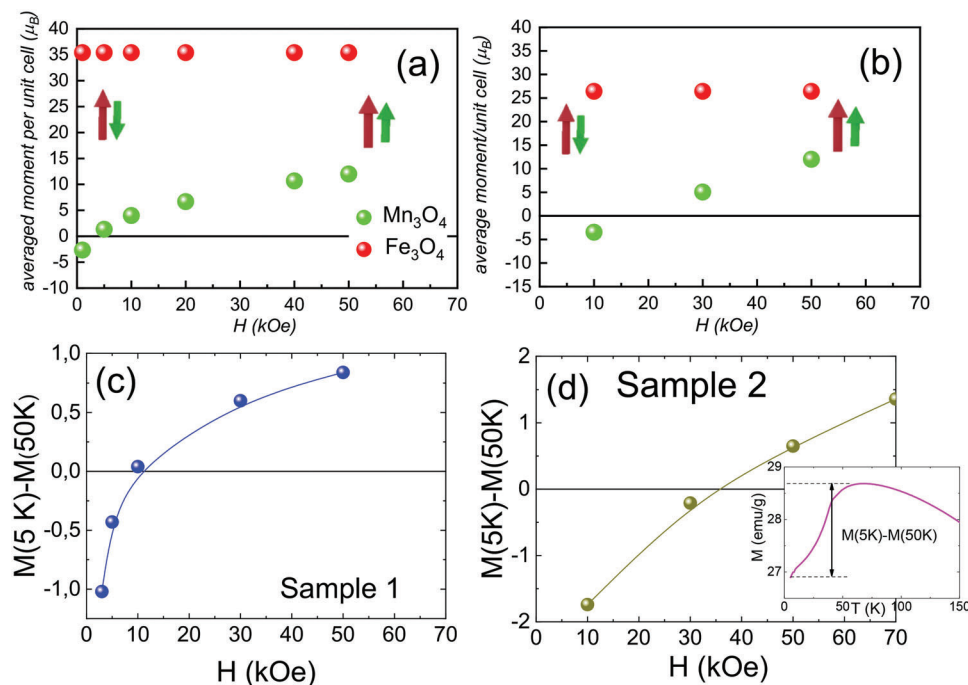


Figure 3. a,b) Dependence of the Fe_3O_4 (red symbols) and Mn_3O_4 (green symbols) moments averaged over the unit cell for a) sample 1 and b) sample 2 on the applied magnetic field. The green and red arrows indicate the orientations of the averaged moments of the Mn_3O_4 and Fe_3O_4 counterparts, respectively. c,d) Evolution of the difference of the magnetizations at 5 and 50 K (i.e., slightly above the bulk T_C of Mn_3O_4 , $T_C = 43$ K) [$M(5\text{K}) - M(50\text{K})$] for diverse applied fields for c) sample 1 and d) sample 2. The lines are guides to the eye. Shown in the inset is an example of the calculation of $M(5\text{K}) - M(50\text{K})$ for sample 2 at 10 kOe, where the arrow shows the difference $M(5\text{K}) - M(50\text{K})$. The error bars (about $\pm 0.7 \mu_B$) in panels (a) and (b), that is, estimates standard deviation from the CrysPy refinement, do not exceed the symbol size.

samples. This behavior is indicative of an antiferromagnetic interface coupling between the Fe_3O_4 and Mn_3O_4 moments at low fields, typical for $\text{Fe}_3\text{O}_4/\text{Mn}_3\text{O}_4$.^[23] However, at increased fields, the averaged moment of Mn_3O_4 changes sign with respect to the one of Fe_3O_4 . This is due to the fact that the antiferromagnetic coupling is overcome, leading to the parallel arrangement of the Fe_3O_4 and Mn_3O_4 moments at high fields. This reorientation is illustrated schematically by arrows in Figure 3a,b. However, as it will be discussed later, one can note that the magnetic order of the Mn_3O_4 phase is more complex than this schematic illustration.

Additionally, the field needed to overcome the antiferromagnetic interface coupling is larger for sample 2 than for sample 1, which should probably be ascribed to dissimilar strengths of the interface coupling in the two samples.^[23]

To illustrate the magnetic configuration obtained from PNPd, magnetization measurements were carried out. The overall magnetic behavior of the samples (Figure 4a,b) is consistent with exchange coupled magnetically soft Fe_3O_4 (high saturation mag-

netization, M_S , low anisotropy) and hard Mn_3O_4 (low M_S , high anisotropy).^[1,23] Namely, sample 2 with a larger amount of Mn_3O_4 exhibits a somewhat lower M_S but a considerably larger coercivity, H_C , and high-field susceptibility, χ_{HF} (Figure 4a,b). However, it is important to emphasize that the hysteresis loops of both samples are rather homogeneous without any obvious differentiated contribution of each of the two phases (Figure 4a,b).

Interestingly, given the large difference between the Néel temperature of Mn_3O_4 [$T_C(\text{Mn}_3\text{O}_4) = 43$ K] and the blocking temperature of the Fe_3O_4 cores [$T_B(\text{Fe}_3\text{O}_4) \approx 250\text{--}300$ K], the temperature dependence of the zero-field cooled (ZFC) magnetization provides some useful information. For both samples, at low fields, the magnetization increases as the temperature is raised from low temperatures to above $T_C(\text{Mn}_3\text{O}_4)$ (Figure 4c,d). This behavior is consistent with the low field antiparallel arrangement observed with PNPd. On the other hand, for large fields, the magnetization decreases as the temperature is increased from low temperatures to above $T_C(\text{Mn}_3\text{O}_4)$ (Figure 4c,d), indicating a

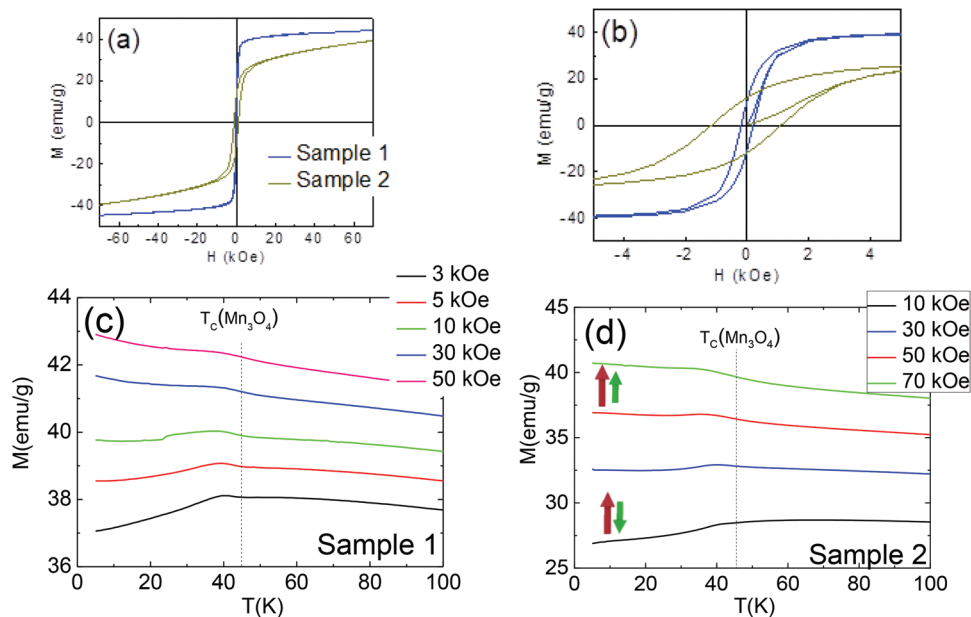


Figure 4. a) Magnetization hysteresis loops at 5 K for samples 1 and 2. b) Enlargement of the hysteresis loops at low fields. c,d) Temperature dependence of the ZFC magnetization for c) sample 1 and d) sample 2 in different applied fields. The bulk Néel temperature of Mn_3O_4 ($T_c = 43$ K) is highlighted by a dashed vertical line. The green and red arrows in (d) indicate the orientation of the moments of the averaged Fe_3O_4 and Mn_3O_4 counterparts, respectively.

reorientation of the averaged Mn_3O_4 moments from antiparallel to parallel to the averaged Fe_3O_4 moments, also in agreement with PNPd.

The difference in the field required to induce the Mn_3O_4 moment reorientation in the two samples observed with PNPd can also be clearly seen in the ZFC magnetization (Figure 4c,d). In fact, the evolution of the difference of the magnetizations measured at 5 and 50 K (see inset in Figure 3d; somewhat indicative of the relative orientation of the moments of the two phases) is comparable to the changes in the Mn_3O_4 moment observed with PNPd (Figure 3c,d).

Nevertheless, it is important to emphasize that magnetization measurements cannot alone confirm the antiferromagnetic interface coupling since other magnetic effects (such as the presence of a spin glass phase) might give rise to a similar behavior. In this regard, the evolution of the averaged moments of the Fe_3O_4 and Mn_3O_4 phases with field observed with PNPd is also consistent with the evolution deduced from element selective XMCD in similar samples, where the Fe-edge signal saturates at rather low fields, while the Mn-edge signal changes sign at intermediate fields.^[23]

Another appealing parameter that can be directly obtained from the PNPd refinement, is the magnetic coherence length. From the peak broadening of the polarized neutron patterns, this length can be estimated even if, due to the reduced statistical accuracy, we simultaneously refined the sum and difference patterns with CrysPy, by assuming the magnetic size (i.e., magnetic coherence length) is the same as the nuclear size (i.e., crystallite size). Indeed, since the crystallite size should not change with field, any changes in the refined size should be related to the evolution of the magnetic coherence length. As can be seen in **Figure 5**, at low fields, the magnetic size of sample 1 remains es-

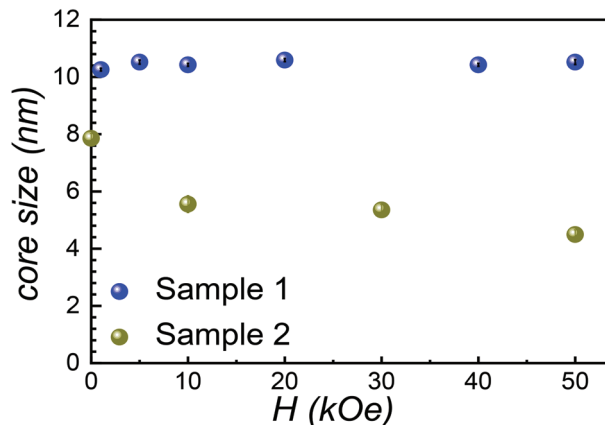


Figure 5. Dependence of the core size of the Fe_3O_4 counterpart of samples 1 and 2 on the applied magnetic field. The error bars (about ± 0.5 nm for sample 1 and ± 2 nm for sample 2), that is, estimates standard deviation from the CrysPy refinement, do not exceed the symbol size.

entially identical to the crystallite size (Table 1) obtained from a separate refinement of the nuclear and magnetic contributions. This indicates that at low fields the core is magnetically homogeneous. This contrasts with single phase nanoparticles, which typically show a magnetically disordered surface layer.^[46,47] Additionally, for sample 1 (with a thin shell and a large core) the coherence length does not significantly change as the field increases (Figure 5).

On the other hand, the magnetic size of the core of sample 2 (at $H = 10$ kOe; Figure 5) is slightly smaller than its magnetic coherence length at $H = 0$ (deduced from the unpolarized beam pattern). Additionally, the magnetic coherence length of sample

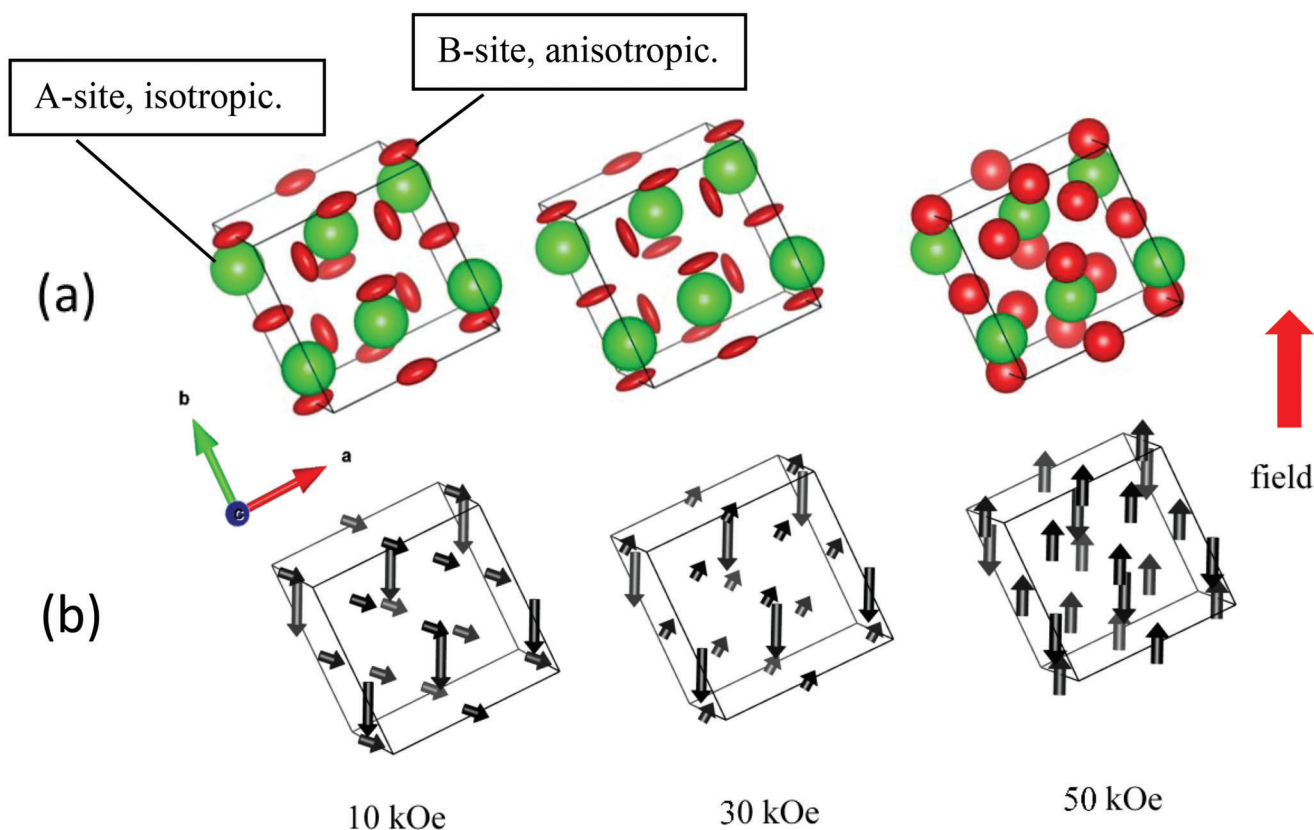


Figure 6. Evolution of the a) local susceptibility ellipsoids (top row) and b) magnetic moments (bottom row) versus applied magnetic field in the Mn_3O_4 shell for sample 2. Tetrahedral A-sites (green) and octahedral B-sites (red). The black arrows show the magnetic moments, calculated according to the standard formulas.^[53,54]

2 seems to further decrease at large fields (Figure 5). This effect is opposite to the one usually observed in single phase nanoparticles, for example, by SANS or Mössbauer spectroscopy, where the coherence length increases at large fields due to the magnetic ordering of the disordered surface layer.^[48,49] The decrease of the coherence length of sample 2 is probably a consequence of the competition between the antiferromagnetic interface coupling and the effect of the applied field (Zeeman energy).^[50] The lower energy state of the $\text{Fe}_3\text{O}_4/\text{Mn}_3\text{O}_4$ interface corresponds to the spins antiferromagnetically coupled. However, as the field increases the Mn_3O_4 moments start to rotate toward an alignment with the applied magnetic field. Consequently, the Fe_3O_4 moments located at the interface suffer a competition between keeping the antiferromagnetic interface coupling and aligning with the applied field, which inevitably leads to some interface magnetic disorder and, hence, a decrease in the coherence length. In sample 1, while a similar effect should occur, the shell is too thin to exert a sufficient torque on the large Fe_3O_4 core to result in any detectable effect within our experimental accuracy. To confirm these effects, Monte Carlo simulations^[51,52] on two different particles analogous to the experiment ones were carried out (see Supporting Information). The simulations confirm that at intermediate fields, where the shell moments are rotating, the spins of the core close to the interface tilt more than the inner spins of the core (Figures S5 and S6, Supporting Information), implying a reduced coherence length. Interestingly, the effects are weaker for

the particles with a larger core and thinner shell, in concordance with the experimental results.

From the refinement of the PNP profiles, the local anisotropy of all sublattices can also be inferred. While unpolarized powder diffraction data deals with ground state magnetic structures in the absence of magnetic field, PNP gives information about the local magnetic moments under magnetic field and allows to estimate the local susceptibility tensor.^[19,31,32,43]

Figures 6a and **6b** show respectively the evolution with the applied field of the local susceptibility tensor and the magnetic moments of the Mn_3O_4 shell of sample 2 for a crystallite with the field applied along its $[1\ 2\ 0]$ direction.

The refinement indicates that the Mn^{2+} (*s*-state, $L = 0$) ions in the tetrahedral A-sites of the Mn_3O_4 lattice are rather insensitive to the magnetic field, that is, the local susceptibility remains roughly constant with the applied field. On the other hand, the moments in the octahedral B-positions rotate to align toward the magnetic field. This implies that while at low fields the magnetic arrangement of the Mn_3O_4 lattice is canted, it evolves toward a collinear arrangement as the field increases. Note, that the induced magnetic moment of each crystallite depends on its orientation with respect to the applied field. This rearrangement of the octahedral moments is at the origin of the evolution of the magnetic properties of these core/shell particles at high fields (i.e., antiparallel versus parallel average moment arrangement between the core and the shell as the field increases).

Remarkably, the local magnetic susceptibility tensor in the octahedral B-site (ellipsoids in Figure 6) changes as the field is increased. This variation from ellipsoids (i.e., anisotropic) to spheres (i.e., isotropic) indicates the evolution of the local anisotropy, that is, how the different magnetic ions respond to the applied field. It is worth mentioning that apart from the single ion anisotropy the inter (and intra) sublattice exchange interactions might be also at the origin of the anisotropy. In particular, the B-site ions, arranged in a frustrated pyrochlore-like lattice,^[55,56] could also be the source of the observed ellipsoid evolution.

3. Conclusions

To summarize, we have systematically explored the use of polarized powder neutron diffraction to unravel the contribution of the two magnetic phases in bi-magnetic Fe₃O₄/Mn₃O₄ core/shell nanoparticles by using the newly developed CrysPy software. Despite the very challenging experimental conditions, quantitative information on both Fe₃O₄ and Mn₃O₄ magnetic phases has been obtained. The evolution of the Fe₃O₄ and Mn₃O₄ signals with the applied field shows that while the moment of the Fe₃O₄ core remains roughly constant, the moment averaged over the unit cell of the Mn₃O₄ shell reorients from antiparallel to parallel to the Fe₃O₄ as the field increases. This reorientation is evidenced also in the changes in the local susceptibility of Mn₃O₄. In addition, the coherence length of the Fe₃O₄ core has been found to decrease at large fields due to the interface disorder induced by the rotation of the averaged moment of the Mn₃O₄ shell. These results open new avenues to obtain valuable information on the individual magnetic properties of each phase in multi-magnetic nanostructured materials by the quantitative refinement of polarized powder neutron diffraction.

4. Experimental Section

Polarized Neutron Powder Diffraction Measurements and Data Analysis: The PNPD experiments were carried out at the D20 diffractometer ($\lambda = 2.4 \text{ \AA}$) of the Institut Laue Langevin (ILL) (sample 1) and at the 6T2 diffractometer ($\lambda = 1.4 \text{ \AA}$) of the Laboratoire Léon Brillouin (LLB) (sample 2). The beam was polarized with a ³He spin filter at D20^[57,58] and a pyrolytic graphite monochromator combined with a supermirror bender at 6T2.

Both experiments were performed in magnetic fields up to 50 kOe after zero field cooling from 300 to 10 K. To avoid any rotation of the powders, the experiments were carried out on tightly packed samples. Note that the refinements did not show any preferred orientation.

The polarized neutrons patterns were fitted using the new software package CrysPy,^[43] specially developed for polarized neutron diffraction data analysis.^[53,54] The definition of different parameters refined by CrysPy can be found in ref.^[43] Note that in PNPD experiments the sum and the difference of the spin-up and spin-down patterns can be refined simultaneously. It is important to highlight that the difference pattern was free from the contribution of any parasitic reflections (e.g., due to the cryostat).

Importantly, the demanding experimental conditions, that is, few tens of mg of sample and heterostructured nanometric system with very thin Mn₃O₄ shells, make the analysis of the results particularly challenging. Thus, certain constraints were used to guarantee the convergence of the fitting procedure:

(i) It was assumed that the local susceptibilities at the A- and B-sites of Fe₃O₄ core were isotropic, which implied that the susceptibility tensor^[43] had diagonal terms only. This approach was justified because the exchange

interactions in magnetite and maghemite, with a Néel temperatures above 850 K, dominated over the magnetic anisotropy.

(ii) For Mn²⁺ (A-site of Mn₃O₄), an anisotropic model due to symmetry limitations had only two refined parameters: $\chi_{xx} = \chi_{yy}$ and χ_{zz} . Preliminary calculations show that it was not possible to refine them individually due to the strong correlation. Therefore, an isotropic model with fixed $\chi_{xx} = \chi_{yy} = \chi_{zz} = 5 \mu_B/B$ was used.

(iii) For Mn³⁺ (B-site of Mn₃O₄) an anisotropic model can have variable parameters χ_{xx} , χ_{yy} , χ_{zz} , and χ_{yz} (the latter defines the inclination of the ellipsoid). The refinement shows that χ_{xx} and χ_{yy} are indistinguishable, and the parameter χ_{yz} cannot be refined reliably (i.e., it diverges). The parameters χ_{yy} (or χ_{xx}) and χ_{zz} are strongly correlated and cannot be refined individually.

(iv) Obviously, the moment in any direction of the applied field cannot exceed the free-ion value. More importantly, there was a magnetic experimental constraint. Namely, the calculated overall moment should be consistent with the experimental magnetization data with only a scalable parameter.

(v) For the sample 2, to reduce the number of variable parameters further it was assumed that the diagonal terms in the susceptibility tensor of the Fe₃O₄ core to be $5 \mu_B/B$ independent of the applied field. This corresponded to a Néel-type magnetic structure with a constant magnetic moment of $5 \mu_B$.

(vi) For the sample 2, the parasitic reflections due to the cryostat were exceedingly large and disallowed the simultaneous fit of the sum and difference patterns. Thus, only the difference pattern (where the parasitic reflections are absent) was fitted using CrysPy. For this sample, the basic parameters of the particles (e.g., lattice parameters, crystallite size, core/shell volume ratio) were obtained from non-polarized powder diffraction measurements performed at the D1B diffractometer of the ILL and analyzed with the FullProf package.^[59]

(vii) The diffraction peaks from a shell were strongly broadened and, consequently, had only a weak effect on the refinement. As a result, the magnetic structure of the shell, despite the above constraints, cannot be inferred with sufficient accuracy only from the refinement of PNPD data. In order to distinguish between the various models (i.e., different terms of the local susceptibility tensors to be refined by CrysPy; including diverse structures that could potentially lead to the effects observed in the magnetization data), an integral overall local susceptibility ellipsoids in the system was calculated, which was proportional to the bulk magnetization of the system. Then the calculated overall magnetization was compared to the magnetization measured using a SQUID (see **Figures 7 and 8**). Note that the values of M obtained from the CrysPy refinement were scaled by a factor ≈ 0.4 to match the ones obtained from SQUID measurements.

As can be seen in Figures S7 and S8, Supporting Information, even small changes in the applied model can have substantial effect on the overall moment (i.e., integrated over all local susceptibility ellipsoids) obtained from the refinement. In the specific case of Figures S7 and S8, Supporting Information, whereas using $\chi_{yy} = -1.8$ the overall moment agrees with the magnetization data, using $\chi_{yy} = -1.4$ led to an exceedingly large moment at low fields.

It was also important to emphasize that for less challenging samples the number of constraints applied to the refinements should be far lower, if any at all. However, the experiment demonstrated that the flipping ratio method can be very enlightening, even in very unfavorable conditions.

Sample Preparation: The Fe₃O₄/Mn₃O₄ core/shell nanoparticles were synthesized in two steps using the seeded growth technique following a previously reported synthesis.^[23] In the first step, Fe₃O₄ nanoparticles were synthesized through thermal decomposition and in the second step, a Mn₃O₄ layer is grown on top of the Fe₃O₄ nanoparticles.

The Fe₃O₄ seeds were synthesized by thermal decomposition of iron(III) oleate.^[60] The growth of the Mn₃O₄ layer onto Fe₃O₄ seeds was performed by injecting a certain amount of Mn acetylacetonate previously heated with oleylamine, oleic acid, 1,2-hexadecanediol, and dibenzyl ether.

The main difference between both samples was in (i) the size of the Fe₃O₄ seeds, which were synthesized in different conditions of precursor concentration and heating rate and (ii) the amount of Mn precursor which in sample 2 was the double of that in sample 1.

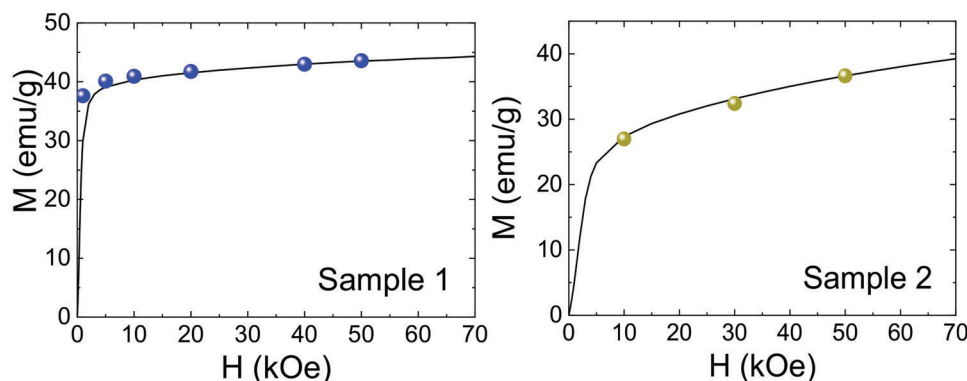


Figure 7. Initial magnetization (solid line; measured by SQUID) and the averaged total magnetic moment (symbols; obtained from the CrysPy refinement $\times 0.4$) for the samples 1 (left) and 2 (right). The error bars, that is, estimates standard deviation from the CrysPy refinement, do not exceed the symbol size.

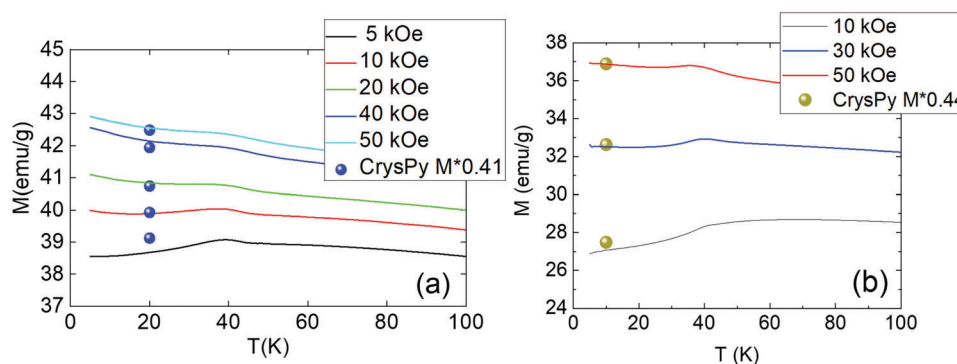


Figure 8. Temperature dependence of the ZFC magnetization for a) sample 1 and b) sample 2 in different applied fields (lines). The symbols correspond to the refined total average magnetic moment. The error bars, that is, estimates standard deviation from the CrysPy refinement, do not exceed the symbol size.

All the particles were purified several times by centrifuging at 10 000 rpm mixing with hexane and acetone.

Nanoparticles of sample 1 were dispersed in n-eicosane to minimize dipolar interactions. 50 mL suspension of nanoparticles in toluene were sonicated for 5 min to prevent any possible sample aggregation. Meanwhile, 5 g of n-eicosane were heated using a heat gun until it became liquid, and then 200 mL were rapidly added to the nanoparticle suspension. The homogeneous suspension was solidified by placing it in iced water.

Note that magnetite (Fe_3O_4) nanoparticles were susceptible to surface oxidation to maghemite ($\gamma\text{-Fe}_2\text{O}_3$). This effect increases with time, especially for small sizes. This is why the core of sample 2, which was smaller in size and was synthesized 7 years ago, oxidized to $\gamma\text{-Fe}_2\text{O}_3$.

Transmission Electron Microscopy Characterization: The morphology of the nanoparticles was characterized by TEM, using a JEOL JEM-1400, operating at 120 kV, and a FEI Tecnai G2 F20 HR(S) TEM microscope (operated at 80 kV to avoid any beam induced damage^[61]). The EELS studies were performed in the latter microscope, equipped with a Quantum GIF EELS spectrometer. Note that only a few nanoparticles were analyzed during the EELS mapping study. Thus, the core sizes and shell thicknesses obtained from this study should be taken as approximate.

Since the particle size distributions were slightly asymmetric, they were fitted using a log-normal distribution. Fits using Gaussian distributions led to comparable particle sizes with similar χ^2 values, thereby confirming the very slight asymmetry of the distribution.

Note that previous high-resolution TEM studies on analogous particles have shown the Mn_3O_4 shell grew coherently on the Fe_3O_4 core with rather sharp interfaces.^[23,61,62]

Magnetization Measurements: The magnetization measurements were carried out on either manually packed powdered samples (samples 1 and 2) or on dispersed nanoparticles in n-eicosane (sample 1) using a SQUID magnetometer (Quantum Design) with a 70 kOe maximum field. The temperature dependence of the magnetization was recorded while warming after ZFC from 300 to 5 K at different fields. The hysteresis loops were carried out at 5 K (using a maximum field of 70 kOe) after ZFC from 300 K.

To properly correlate the PNPD and magnetometry data, both experiments were carried out under the same conditions, that is, using tightly packed powders. However, for completeness, some magnetometry experiments on powders dispersed in n-eicosane (to minimize dipolar interactions)^[10,17,63] were also carried out for sample 1 (see Supporting Information).

X-Ray Diffraction: Powder X-ray diffraction patterns were measured with a wavelength of 0.4131 Å at the BL04-beamline of the ALBA Synchrotron and with a Panalytical X'Pert Pro diffractometer with $\text{CuK}\alpha$ radiation.

Statistical Analysis

Note that the data presentation is given as mean $\pm \sqrt{\text{variance}}$ for TEM particle sizes, and average (estimated standard deviation) for other parameters. The errors for the particle size distribution were obtained by means of non-linear fits using Origin 8.5, using at least 200 particles. The errors related to the neutron diffraction refinements were obtained from the estimated standard deviation calculated by the FullProf and CrysPy programs, which corresponded to one sigma error in a normal distribution with a 68% confidence interval.

Supporting Information

Supporting Information is available from the Wiley Online Library or from the author.

Acknowledgements

I.V.G. acknowledges financial support from the Russian Foundation for Basic Research under Grant No 20-02-00109. A.G.R. and J.N. acknowledge financial support from the grants PID2019-106229RB-I0 funded by MCIN/AEI/10.13039/501100011033 and 2021-SGR-00651 from Generalitat de Catalunya. I.K. and A.G. acknowledge the European Union's H2020 research and innovation program, Grant agreement No 871072. A.G.R. acknowledges financial support from RYC2019-027449-I funded by MCIN/AEI/10.13039/501100011033. ICN2 is funded by the CERCA programme/Generalitat de Catalunya. The ICN2 is supported by the CEX2021-001214-S grant funded by MCIN/AEI/10.13039/501100011033. M.E. acknowledges the grants RYC2018-024396-I and PID2019-106165GB-C22 funded by MCIN/AEI/10.13039/501100011033 and by "ESF Investing in your future." A.L.O. acknowledges financial support from the grants PID2021-122613OB-I00 funded by MCIN/AEI/10.13039/501100011033 and PJUPNA2020 from Universidad Pública de Navarra. The authors thank ILL (D1B <https://doi.org/10.5291/ILL-DATA.5-31-2650>, D20 <https://doi.org/10.5291/ILL-DATA.5-32-932>), LLB and ALBA for the provision of beam-time.

Conflict of Interest

The authors declare no conflict of interest.

Data Availability Statement

The data that support the findings of this study are available from the corresponding author upon reasonable request.

Keywords

antiferromagnetic coupling, core/shell nanoparticles, Fe_3O_4 , magnetic coherence length, Mn_3O_4 , polarized neutron powder diffraction

Received: December 31, 2022
Revised: May 10, 2023
Published online: June 30, 2023

- [1] A. Lopez-Ortega, M. Estrader, G. Salazar-Alvarez, A. G. Roca, J. Nogues, *Phys. Rep.* **2015**, 553, 1.
- [2] F. Liu, Y. Hou, S. Gao, *Chem. Soc. Rev.* **2014**, 43, 8098.
- [3] O. Gutfleisch, *J. Phys. D: Appl. Phys.* **2000**, 33, R157.
- [4] G. W. Qin, Y. P. Ren, N. Xiao, B. Yang, L. Zuo, K. Oikawa, *Int. Mater. Rev.* **2009**, 54, 157.
- [5] L. Fallarino, B. J. Kirby, E. E. Fullerton, *J. Phys. D: Appl. Phys.* **2021**, 54, 303002.
- [6] J. A. De Toro, D. P. Marques, P. Muñiz, V. Skumryev, J. Sort, D. Givord, J. Nogues, *Phys. Rev. Lett.* **2015**, 115, 057201.
- [7] F. Fabris, E. Lima Jr., C. Quinteros, L. Neñer, M. Granada, M. Sirena, R. D. Zysler, H. E. Troiani, V. Laborán, F. Rivadulla, E. L. Winkler, *Phys. Rev. Appl.* **2019**, 11, 054089.
- [8] J. Sort, V. Langlais, S. Doppiu, B. Dieny, S. Suriñach, J. S. Muñoz, M. D. Baró, C. Laurent, J. Nogues, *Nanotechnology* **2004**, 15, S211.
- [9] A. Omelyanchik, S. Villa, M. Vasilakaki, G. Singh, A. M. Ferretti, A. Ponti, F. Canepa, G. Margaritis, K. N. Trohidou, D. Peddis, *Nanoscale Adv* **2021**, 3, 6912.
- [10] E. H. Sanchez, M. Vasilakaki, S. S. Lee, P. S. Normile, G. Muscas, M. Murgia, M. S. Andersson, G. Singh, R. Mathieu, P. Nordblad, P. C. Ricci, D. Peddis, K. N. Trohidou, J. Nogues, J. A. De Toro, *Chem. Mater.* **2020**, 32, 969.
- [11] P. Gorria, D. Martínez-Blanco, J. A. Blanco, M. J. Pérez, A. Hernando, L. Fernández Barquín, R. I. Smith, *Phys. Rev. B* **2005**, 72, 01440.
- [12] I. V. Golosovsky, G. Salazar-Alvarez, A. Lopez-Ortega, M. A. Gonzalez, J. Sort, M. Estrader, S. Suriñach, M. D. Baró, J. Nogues, *Phys. Rev. Lett.* **2009**, 102, 247201.
- [13] M. Yuan, B. Zhao, C. Yang, K. Pei, L. Wang, R. Zhang, W. You, X. Liu, X. Zhang, R. Che, *Adv. Funct. Mater.* **2022**, 32, 2203161.
- [14] A. López-Ortega, M. Estrader, G. Salazar-Alvarez, S. Estradé, I. V. Golosovsky, R. K. Dumas, D. J. Keavney, M. Vasilakaki, K. N. Trohidou, J. Sort, F. Peiró, S. Suriñach, M. D. Baró, J. Nogues, *Nanoscale* **2012**, 4, 5138.
- [15] C. Romero-Muñiz, V. Franco, A. Conde, *Appl. Phys. Lett.* **2013**, 102, 082402.
- [16] E. Lottini, A. López-Ortega, G. Bertoni, S. Turner, M. Meledina, G. Van Tendeloo, C. de Julián Fernández, C. Sangregorio, *Chem. Mater.* **2016**, 28, 4214.
- [17] J. A. De Toro, M. Vasilakaki, S. S. Lee, M. S. Andersson, P. S. Normile, N. Yaacoub, P. Murray, E. H. Sánchez, P. Muñiz, D. Peddis, R. Mathieu, K. Liu, J. Geshev, K. N. Trohidou, J. Nogués, *Chem. Mater.* **2017**, 29, 8258.
- [18] S. M. Yusuf, A. Kumar, *Appl. Phys. Rev.* **2017**, 4, 031303.
- [19] R. J. Harrison, *Rev. Miner. Geochem.* **2006**, 63, 113.
- [20] M. Estrader, A. López-Ortega, I. V. Golosovsky, S. Estradé, A. G. Roca, G. Salazar-Alvarez, L. López-Conesa, D. Tobia, E. Winkler, J. D. Ardisson, W. A. A. Macedo, A. Morphis, M. Vasilakaki, K. N. Trohidou, A. Gukasov, I. Mirebeau, O. L. Makarova, R. D. Zysler, F. Peiró, M. D. Baró, L. Bergström, J. Nogues, *Nanoscale* **2015**, 7, 3002.
- [21] G. van der Laan, A. I. Figueroa, *Coord. Chem. Rev.* **2014**, 277–278, 95.
- [22] X. M. Cheng, D. J. Keavney, *Rep Prog Phys* **2012**, 75, 026501.
- [23] M. Estrader, A. López-Ortega, S. Estradé, I. V. Golosovsky, G. Salazar-Alvarez, M. Vasilakaki, K. N. Trohidou, M. Varela, D. C. Stanley, M. Sinko, M. J. Pechan, D. J. Keavney, F. Peiró, S. Suriñach, M. D. Baró, J. Nogues, *Nat. Commun.* **2013**, 4, 2960.
- [24] D. Honecker, M. Bersweiler, S. Erokhin, D. Berkov, K. Chesnel, D. A. Venero, A. Qdemat, S. Disch, J. K. Jochum, A. Michels, P. Bender, *Nanoscale Adv* **2022**, 4, 1026.
- [25] K. L. Krycka, J. A. Borchers, M. Laver, G. Salazar-Alvarez, A. Lopez-Ortega, M. Estrader, S. Suriñach, M. D. Baró, J. Sort, J. Nogues, *J. Appl. Phys.* **2013**, 113, 17B531.
- [26] S. D. Oberdick, A. Abdelgawad, C. Moya, S. Mesbahi-Vasey, D. Kepaptsoglou, V. K. Lazarov, R. F. Evans, D. Meilak, E. Skoropata, J. Van Lierop, I. Hunt-Isaak, H. Pan, Y. Ijiri, K. L. Krycka, J. A. Borchers, S. A. Majetich, *Sci. Rep.* **2018**, 8, 3425.
- [27] D. S. Song, Z. Q. Wang, X. Y. Zhong, J. Zhu, *Chin. Phys. B* **2018**, 27, 056801.
- [28] D. del-Pozo-Bueno, M. Varela, M. Estrader, A. López-Ortega, A. G. Roca, J. Nogues, F. Peiró, S. Estradé, *Nano Lett.* **2021**, 21, 6923.
- [29] C. L. Bianchi, R. Djellabi, A. Ponti, G. S. Patience, E. Falletta, *Can. J. Chem. Eng.* **2021**, 99, 2105.
- [30] A. S. Kamzin, I. M. Obaidat, A. A. Valliulin, V. G. Semenov, I. A. Al-Omari, *Phys. Solid State* **2020**, 62, 1933.
- [31] O. Rivin, H. Shaked, A. Gukasov, E. N. Caspi, *J. Neutron Res.* **2015**, 18, 13.
- [32] E. Lelièvre-Berna, A. S. Wills, E. Bourgeat-Lami, A. Dee, T. Hansen, P. F. Henry, A. Poole, M. Thomas, X. Tonon, J. Torregrossa, K. H. Andersen, F. Bordenave, D. Jullien, P. Mouveau, B. Guéard, G. Manzin, *Meas. Sci. Technol.* **2010**, 21, 055106.

- [33] D. Luneau, B. Gillon, *Magnetochemistry* **2021**, *7*, 158.
- [34] A. Borta, B. Gillon, A. Gukasov, A. Cousson, D. Luneau, E. Jeanneau, I. Ciumacov, H. Sakiyama, K. Tone, M. Mikuriya, *Phys. Rev. B* **2011**, *83*, 184429.
- [35] K. Ridier, A. Mondal, C. Boilleau, O. Cador, B. Gillon, G. Chaboussant, B. Le Guennic, K. Costuas, R. Lescouëzec, *Angew. Chem., Int. Ed.* **2016**, *55*, 3963.
- [36] O. Rivin, E. N. Caspi, H. Etdedgui, H. Shaked, A. Gukasov, *Phys. Rev. B* **2013**, *88*, 054430.
- [37] E. Brok, K. Lefmann, P. P. Deen, B. Lebech, H. Jacobsen, G. J. Nilsen, L. Keller, C. Frandsen, *Phys. Rev. B* **2015**, *91*, 014431.
- [38] D. Lin, A. C. Nunes, C. F. Majkrzak, A. E. Berkowitz, *J. Magn. Magn. Mater.* **1995**, *145*, 343.
- [39] S. Sabyasachi, M. Patra, S. Majumdar, S. Giri, S. Das, V. S. Amaral, O. Iglesias, W. Borghols, T. Chatterji, *Phys. Rev. B* **2012**, *86*, 104416.
- [40] H. Hiraka, K. Ohoyama, Y. Ogata, T. Ogawa, R. Gallage, N. Kobayashi, M. Takahashi, B. Gillon, A. Gukasov, K. Yamada, *Phys. Rev. B* **2014**, *90*, 134427.
- [41] C. H. Wang, S. N. Baker, M. D. Lumsden, S. E. Nagler, W. T. Heller, G. A. Baker, P. D. Deen, L. M. D. Cranswick, Y. Su, A. D. Christianson, *Phys. Rev. B* **2011**, *83*, 214418.
- [42] L. Chang, B. D. Rainford, J. R. Stewart, C. Ritter, A. P. Roberts, Y. Tang, Q. Chen, *J. Geophys. Res.* **2009**, *114*, B07101.
- [43] I. A. Kibalin, A. Gukasov, *Phys. Rev. Res.* **2019**, *1*, 033100.
- [44] E. A. Klahn, C. Gao, B. Gillon, A. Gukasov, X. Fabrèges, R. O. Piltz, S. D. Jiang, J. Overgaard, *Chem. - Eur. J.* **2018**, *24*, 16576.
- [45] I. A. Kibalin, F. Damay, X. Fabrèges, A. Gukasov, *Phys. Rev. Res.* **2020**, *2*, 033509.
- [46] S. Disch, E. Wetterskog, R. P. Hermann, A. Wiedenmann, U. Vainio, G. Salazar-Alvarez, L. Bergström, T. Brückel, *New J Phys* **2012**, *14*, 013025.
- [47] R. H. Kodama, A. E. Berkowitz, E. J. McNiff Jr, S. Foner, *Phys. Rev. Lett.* **1996**, *77*, 394.
- [48] D. Zákutná, D. Nižňanský, L. C. Barnsley, E. Babcock, Z. Salhi, A. Feoktystov, D. Honecker, S. Disch, *Phys. Rev. X* **2020**, *10*, 031019.
- [49] H. R. Rechenberg, E. C. Sousa, J. Depeyrot, M. H. Sousa, R. Aquino, F. A. Tourinho, R. Perzynski, *Hyperfine Interact.* **2008**, *184*, 9.
- [50] C. Leighton, J. Nogues, H. Suhl, I. K. Schuller, *Phys. Rev. B* **1999**, *60*, 12837.
- [51] E. Eftaxias, M. Vasilakaki, K. N. Trohidou, *Mod. Phys. Lett. B* **2007**, *21*, 1169.
- [52] K. Trohidou, M. Vasilakaki, in *Applications of Monte Carlo Method in Science and Engineering* (Ed.: S. Mordechai), InTechOpen, London **2011**, pp. 513–538.
- [53] A. Gukasov, P. J. Brown, *J. Phys.: Condens. Matter* **2002**, *14*, 8831.
- [54] A. Gukasov, P. J. Brown, *J. Phys.: Condens. Matter* **2010**, *22*, 502201.
- [55] A. Kuriki, Y. Moritomo, S. Xu, K. Ohoyama, K. Kato, A. Nakamura, *J. Phys. Soc. Jpn.* **2003**, *72*, 458.
- [56] S. Pal, S. Lal, *Phys. Rev. B* **2017**, *96*, 075139.
- [57] E. Lelièvre-Berna, A. Ioffe, *J. Neutron Res.* **2009**, *20*, 30.
- [58] J. Dreyer, L. P. Regnault, E. Bourgeat-Lami, E. Lelièvre-Berna, S. Pujol, F. Thomas, M. Thomas, F. Tasset, *Nucl. Instrum. Methods Phys. Res., Sect. A* **2000**, *449*, 638.
- [59] J. Rodríguez-Carvajal, *Phys. B: Condens. Matter* **1993**, *192*, 55.
- [60] J. Park, K. An, Y. Hwang, J. G. Park, H. J. Noh, J. Y. Kim, J. H. Park, N. M. Hwang, T. Hyeon, *Nat. Mater.* **2004**, *3*, 891.
- [61] M. A. Roldan, A. Mayence, A. López-Ortega, R. Ishikawa, J. Salafranca, M. Estrader, G. Salazar-Alvarez, M. D. Baró, J. Nogues, S. J. Pennycook, M. Varela, *Chem. Eng. J.* **2021**, *405*, 126820.
- [62] P. Torruella, A. Ruiz-Caridad, M. Walls, A. G. Roca, A. Lopez-Ortega, J. Blanco-Portals, L. Lopez-Conesa, J. Nogués, F. Peiro, S. Estrade, *Nano Lett.* **2018**, *18*, 5854.
- [63] E. H. Sanchez, M. Vasilakaki, S. S. Lee, P. S. Normile, M. S. Andersson, R. Mathieu, A. Lopez-Ortega, B. P. Pichon, D. Peddis, C. Binns, P. Nordblad, P. C. Ricci, K. N. Trohidou, J. Nogues, J. A. De Toro, *Small* **2022**, *18*, 2106762.